Global force and moment in rectangular tanks through a modal method for wave sloshing

M. Antuono [a,b,*], C. Lugni [a,b]

[a]*CNR-INSEAN, Marine Technology Research Institute, Rome, Italy*
[b]*AMOS, NTNU, Dept. of Marine Technology, Trondheim, Norway*

Abstract

Basing on a modal description of the sloshing phenomenon, formulas for the global force and moment acting on two-dimensional rectangular tanks are proposed. These are extensively validated through comparison with experimental data for roll motions at different angles of excitement. Moreover, to extend the applicability of the modal method to the most violent breaking cases, a diffusive variant of the scheme is proposed. This relies on the use of a proper diffusive term in the continuity equation and allows for the overcoming of some numerical issues related to the sloshing dynamics in very shallow waters. Finally, a qualitative description of the interaction between diffusion, dispersion and nonlinearities has been proposed for the present modal scheme, along with a physical interpretation of the diffusive term.

Key words: Sloshing dynamics, Generalized forces, Modal methods

1 Introduction

Sloshing is the resonant phenomenon of the liquid motion in a tank excited by an external forcing. Even small excitation amplitudes can induce large free-surface deformation when the forcing frequency is close to the lowest natural sloshing frequency. This is of concern for liquid transportation in ship carrier and LNG ship.

Depending on the excitation features and the filling depth ratio h_0^*/L^*, with h_0^* the water depth and L^* the tank length, several scenarios may occur. As described in Faltinsen and Timokha (2009), nonlinear standing waves characterize the internal wave evolution at high filling ratios, i.e. $h_0^*/L^* > 0.25$. As a consequence of the

---

* Corresponding author: *Tel.: +39 06 50 299 339; Fax: +39 06 50 70 619.*
  Email address: `matteo.antuono@cnr.it` (M. Antuono).

strong runup at the lateral walls and, however for large filling level, tank roof impacts, possibly with large gas cavity entrapped, may happen (e.g. Abrahamsen and Faltinsen 2011). Near the critical depth, that is at $h_0^*/L^* \approx 0.3368$, nonlinear violent free-surface deformation originates breaking waves, rotational flow, super- and sub-harmonic behaviours (see, for example, Colagrossi et al. 2004).

Conversely, at low filling depth, i.e. $h_0^*/L^* < 0.1 - 0.15$, a breaking bore travels back and forth in the tank (e.g. Bouscasse et al. 2013), inducing rotational flow and viscous diffusion. The occurrence of the bore has been explained in Faltinsen and Timokha (2009) as a shock wave phenomenon, consequence of a *commensurate* spectrum characterizing the shallow water resonance in a tank. This means that all the sloshing natural frequencies are multiples of the lowest natural frequency and are nonlinearly excited by the harmonic excitation of the lowest mode (i.e. secondary resonance, Faltinsen and Timokha 2009). The interaction of the breaking wave with lateral walls causes large local loads (see, for example, Lugni et al. 2006, 2010b,a), and hydroelastic effects when the typical temporal duration of the local load is comparable with a natural period of the structural mode contributing to large local stressing (e.g. Lugni et al. 2014). At intermediate depth, that is $0.1 - 0.15 < h_0^*/L^* < 0.25$, a nearly-commensurate spectrum, more similar to the shallow water case, or a non-commensurate spectrum, more similar to the high-filling depth case, can be activated, depending on the natural frequencies for which dispersion matters (e.g. Faltinsen and Timokha 2002).

The above observations strongly influence the choice of the suitable mathematical model to be used on each regime. Although at high and intermediate filling depth, the nonlinear multimodal theory by Faltinsen and Timokha (2009) is a reliable and extremely efficient tool for the description of the sloshing flows, it becomes less accurate for the shallow water case and even not converging for really shallow depth conditions. In any case, it fails when wave breaks.

A reliable approach for the description of the sloshing motion in shallow water conditions is based on the use of depth-averaged equations and on their reformulation as a modal scheme. A first pioneering work in this direction is that of Hill (2003) which, however, is limited to the analysis of the sway motion in the neighbourhood of the first resonant frequency. A more general result is given in Antuono et al. (2012a) where a generic two-dimensional motion is considered, along with the description of a coherent inclusion of the forcing terms in the depth-averaged equations. The above schemes are both limited to the modelling of non-breaking waves and, consequently, can only describe the evolution of rather weak sloshing phenomena. This issue is overcome in the work of Antuono et al. (2014) where a modal scheme based on the depth-averaged equations of Antuono and Brocchini (2013) is implemented along with a semi-analytical solution for the vorticity injected at the free-surface during wave breaking. The above model provides a fairly good match with experimental measurements for moderate wave breaking.

In this context, the aim of the present contribution is the derivation of proper formulas for global forces and momentum and for the consequent evaluation of the loads on the tank, this being a missing aspect in the work of Antuono et al. (2014). This is a requisite for enabling a successful coupling between an efficient sloshing model and an external flow solver for ship seakeeping and stability (Rognebakke and Faltinsen 2003). Potential flow schemes for the dynamic behavior of a marine vessel in waves are commonly used for both the design and research purposes (Greco and Lugni 2012), providing highly efficient and accurate alternatives to the use of the time consuming CFD schemes. However, a drastic reduction of the efficiency happens when potential schemes are coupled with a CFD solver used to reproduce the internal flow, i.e. as for the sloshing flows in the tank of a LNG carrier (Kim et al. 2007), or in an antirolling tank of a fishing vessel. On the other hand, too simplistic models, e.g lumped mass model, can lead to inaccurate solutions with loss of precision (Fonfach et al. 2016). The capability of solving efficiently and accurately the internal loads induced by sloshing flows becomes then a fundamental step for the solution of complex problems with a limited computational effort and with a high level of reliability.

Sloshing phenomena in shallow water conditions are important in LNG carriers, when these travel in almost off-load conditions, on the deck of fishing vessels, on the deck of offshore supply vessels, and in wing fuel tanks of aircraft; however, they are usually 3D problems. Despite the 2D approximation, the present model can be used in several practical problems. A relevant application is the design of a free-surface antirolling tank for a fishing vessel. When the lowest natural sloshing frequency is tuned to be close to the roll natural period of the boat, the sloshing-induced roll moment damps the roll oscillation of the vessel and prevents parametric instability (Ghamari et al. 2017). Since the resonant flow within a free-surface antirolling tank is characterized by a hydraulic jump travelling back and forth, a nonlinear shallow water model is required to predict the hydrodynamic flow and the induced loads. Further, the elongated shape of the tank, i.e. its breadth is much larger than the width, enables the use of a 2D model as a good compromise. Another interesting application is the prediction of the sloshing flow behaviour within the dock of a landing ship, i.e. a warfare ship with a dock used for the launching of landing crafts and amphibious boats. The high computational efficiency along with a good accuracy of the algorithm developed, are the fundamental prerequisites to build a simulator for training purpose.

To extend the use of the proposed formulas for global forces and momentum to practical naval problems, we also broaden the applicability of the modal scheme of Antuono et al. (2014) to more violent sloshing phenomena. This latter point is achieved by introducing a diffusive term in the continuity equation of the model, following the approach described in Molteni and Colagrossi (2009); Antuono et al. (2010, 2012b) in the framework of the Smoothed Particle Hydrodynamics (SPH). At the same time, we provide a physical interpretation of the diffusive term and a qualitative description of its interaction with dispersion and nonlinearities of the
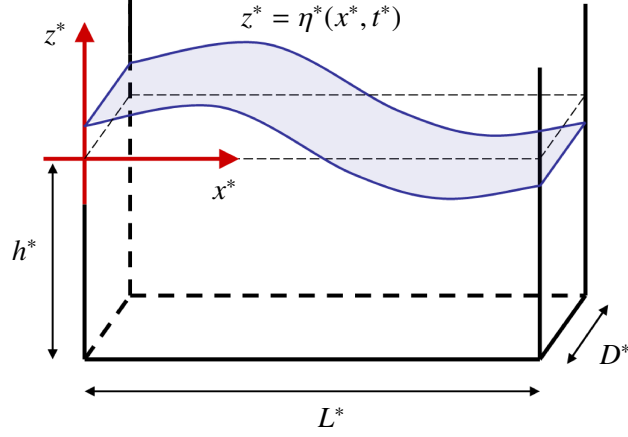
3

Fig. 1. Sketch of the tank and of the frame of reference.

modal scheme. Finally, the proposed formulas and the diffusive variant of the modal scheme are extensively validated through comparison with the experimental data obtained at the CNR-INSEAN Sloshing Lab.

2 The sloshing model

Hereinafter, unstarred variables indicate dimensionless quantities, while starred variables indicate dimensional ones. The frame of reference is that of the tank and x^* and z^* indicate the horizontal and vertical coordinates respectively (see figure 1). The basic model is that described in Antuono et al. (2014). We denote by e_0^* and h_0^* the reference wave amplitude and the mean water depth. Then, ϵ indicates the nonlinearity parameter (i.e. $\epsilon = e_0^*/h_0^*$) and $\mu = h_0^*/L^*$ is the dispersive parameter (here, L^* is the tank length). Denoting by g^* the gravity acceleration, the adopted scaling reads:

$$x^* = L^* x \qquad z^* = h_0^* z \qquad t^* = \frac{L^*}{\sqrt{g^* h_0^*}} t \qquad U^* = \epsilon \sqrt{g^* h_0^*}\, U ,$$

$$\eta^* = e_0^* \eta \qquad h^* = h_0^* h \qquad \omega^* = \epsilon \sqrt{\frac{g^*}{h_0^*}}\, \omega \qquad \nu_T^* = \mu h_0^* \sqrt{g^* h_0^*}\, \nu_T ,$$

where U is the (horizontal) depth-averaged velocity, ω^* is the vorticity and ν_T^* is the turbulent viscosity. The governing equations of the sloshing model have been obtained from the work of Antuono and Brocchini (2013) by approximating their scheme to the order $\mathcal{O}(\epsilon \mu^2, \mu^4)$. The continuous (dimensionless) equations are:

4

$$\begin{cases} \eta_t + (dU)_x = 0, \\\\ U_t + \epsilon U U_x - f_3(t)\,\eta_x - \dfrac{\mu^2 h^2}{3}\,U_{xxt} + \dfrac{\mu^2}{h}\int_{-h}^{\epsilon\eta}\mathrm{d}z\int_z^{\epsilon\eta}\mathrm{d}\zeta\int_\zeta^{\epsilon\eta}R_{xxt}\,\mathrm{d}\xi + \\\\ \quad + \dfrac{\epsilon}{d}\left[\int_{-h}^{\epsilon\eta}R^2\,\mathrm{d}z\right]_x - 4\,\nu_T\,\mu^2\,U_{xx} - 4\,\nu_T\,\dfrac{\mu^2}{h}\int_{-h}^{\epsilon\eta}R_{xx}\,\mathrm{d}z + \\\\ \quad - \nu_T\,\dfrac{\mu^2}{h}\int_{-h}^{\epsilon\eta}\left[\int_z^{\epsilon\eta}\omega\,\mathrm{d}\zeta\right]_{xx}\mathrm{d}z = \gamma(x)\,\dfrac{f_1(t)}{\mu} + \mathcal{O}(\epsilon\mu^2,\mu^4), \end{cases} \tag{1}$$

where $d = \epsilon\eta + h$ is the total water depth and $\gamma(x)$ is the modulating term described in Antuono et al. (2012a). Symbols f_1 and f_3 respectively indicate the horizontal and vertical components of the exciting force and are included inside the governing equations by using the same procedure described in Antuono et al. (2012a). Since we just consider two-dimensional motions, the transversal component, namely f_2, is null. The expressions of f_1, f_3 and $\gamma(x)$ are detailed later in the present section. The turbulent terms have been expressed through a Boussinesq closure and the turbulent viscosity, ν_T, has been assumed to be constant in the liquid field. This is a simple but reliable and accurate enough approach. Specifically, we set $\nu_T = 0.08/\mu$ in accordance with Antuono et al. (2014) where an extensive tuning of such parameter was realized. Finally, the term R reads:

$$R = -\int_z^{\epsilon\eta}\omega\,\mathrm{d}\zeta + \frac{1}{d}\int_{-h}^{\epsilon\eta}\mathrm{d}z\int_z^{\epsilon\eta}\omega\,\mathrm{d}\zeta. \tag{2}$$

Following the work of Antuono et al. (2014), we expand the dependent variables in Fourier series:

$$\eta = \sum_{n=1}^{\infty} H_n(t)\,\cos(n\pi x) \qquad U = \sum_{n=1}^{\infty} U_n(t)\,\sin(n\pi x) \tag{3}$$

$$\omega = \sum_{n=1}^{\infty}\sum_{m=1}^{\infty} \phi_{n,m}(t)\,\sin(n\pi x)\,\sin(m\pi y) \qquad \text{with} \quad y = -\frac{\epsilon\eta - z}{d}. \tag{4}$$

The variable y is used to simplify the assignment of the vorticity injection at the free surface. These expressions are rewritten by using complex numbers as follows:

5

$$\eta = \sum_{n \in \mathbb{Z}} \frac{H_n(t)}{2} e^{in\pi x} \qquad U = \sum_{n \in \mathbb{Z}} \frac{U_n(t)}{2i} e^{in\pi x} \tag{5}$$

$$\omega = \sum_{n \in \mathbb{Z}} \frac{e^{in\pi x}}{2i} \sum_{m=1}^{+\infty} \phi_{n,m}(t) \, \sin(m\pi y) \tag{6}$$

with $H_{-n} = H_n$, $U_{-n} = -U_n$ and $\phi_{-n,m} = -\phi_{n,m} \; \forall m \in \mathbb{N}$. Further, we set $H_0 = 0$, this meaning that the still water level is set equal to zero. As the system (1) is expressed in terms of depth-averaged quantities, the wave breaking is approximated through appropriate models for coastal dynamics. While the wave overturning cannot be explicitly described by such models, they are sufficiently accurate to predict the average dissipation induced by the vortical and turbulent structures. In particular, following the work of Veeramony and Svendsen (2000), the vorticity is assumed to be known and is modelled through an approximate analytic solution which describes the wave-breaking occurrence and the related injection of the vorticity at the free surface. Specifically, the analytic solution for $\phi_{n,m}$ is described in Antuono et al. (2014) and, for the sake of brevity, is not reported here. Finally, the modulating term $\gamma(x)$ is represented as follows:

$$\gamma(x) = \sum_{n \in \mathbb{Z}} \frac{\gamma_n}{2i} e^{in\pi x} \qquad \text{with} \quad \gamma_n = -2 \left[\frac{(-1)^n - 1}{n\pi} \right] \quad \text{for } n \in \mathbb{Z} \backslash \{0\},$$

and $\gamma_0 = 0$. More details can be found in Antuono et al. (2012a). Substituting the above expressions in system (1) we obtain the following modal scheme:

$$
\begin{cases}
\dot{H}_n + n\pi h U_n + \epsilon \dfrac{n\pi}{4} \sum_{p \in \mathbb{Z}} \left[H_p U_{n-p} + H_{n-p} U_p \right] = 0, \\[4mm]
\dot{U}_n \left(1 + \dfrac{\mu^2 n^2 \pi^2 h^2}{3} \right) + n\pi f_3 H_n + \beta_n U_n + \epsilon \dfrac{n\pi}{4} \sum_{p \in \mathbb{Z}} U_p U_{n-p} + \mu^2 n^2 \pi^2 \sum_{m=1}^{+\infty} \dfrac{\dot{\phi}_{n,m}}{(m\chi)^3} + \\[4mm]
+ \epsilon \dfrac{n\pi}{4} \sum_{p \in \mathbb{Z}} \sum_{m=1}^{+\infty} \dfrac{\phi_{p,m} \phi_{n-p,m}}{(m\chi)^2} + 4\nu_T \mu^2 n^2 \pi^2 U_n - \nu_T \mu^2 n^2 \pi^2 \sum_{m=1}^{+\infty} \dfrac{\phi_{n,m}}{(m\chi)} = \gamma_n \dfrac{f_1}{\mu}
\end{cases}
$$

where $\chi = \pi/h$ is the (dimensionless) wave number associated with the vertical direction and:

$$\beta_n = \frac{1}{h} \left(1 + \frac{2h^*}{D^*} \right) \left(\frac{\nu n\pi \sqrt{h}}{2} \right)^{1/2} + 4\nu \mu^2 n^2 \pi^2, \tag{7}$$

where $\nu = \nu^* / (\mu h_0^* \sqrt{g^* h_0^*})$ is the dimensionless kinematic viscosity of the liquid and D^* is the tank breadth. As explained in Antuono et al. (2012a), the coefficient β_n

takes into account the dissipation caused by the boundary layer along the tank wall and the viscous dissipation inside the liquid bulk (see, for example, Lamb 1945; Antuono and Colagrossi 2013). Conversely, the dissipation due to turbulence is modelled through the term $(4\nu_T \mu^2 n^2 \pi^2 U_n)$. In any case, since turbulence is mainly generated by wave breaking, this term is switched on only when breaking occurs, otherwise it is set to zero. The conditions for the wave-breaking occurrence are described in Antuono et al. (2014). Finally, we briefly recall the expressions for the forces f_1 and f_3:

$$f_1(t) = -\sin\theta - a_{0,1}\cos\theta - a_{0,3}\sin\theta + \mu^2\ddot{\theta}(z_C - z_0) + \mu\dot{\theta}^2(x_C - x_0) + 2\mu^2\dot{\theta}w_C,$$

$$f_3(t) = -\cos\theta + a_{0,1}\sin\theta - a_{0,3}\cos\theta - \mu\ddot{\theta}(x_C - x_0) + \mu^2\dot{\theta}^2(z_C - z_0) - 2\mu\dot{\theta}u_C,$$

where $\boldsymbol{a}_0 = (a_{0,1}, 0, a_{0,3})$ is the tank acceleration and $\dot{\boldsymbol{\Omega}} = (0, \dot{\theta}, 0)$ is its rotation (here θ is the angle between the horizontal axis of the frame of reference of the tank and the horizontal axis of the fixed frame of reference). Here, x_C and z_C are the coordinates of the mass center of the tank, u_C and w_C its velocity components and x_0 and z_0 the coordinates of the rotation center. Specifically:

$$x_C = \frac{1}{2} + \sum_{n=1}^{+\infty} \frac{[-1 + (-1)^n]}{\pi^2 n^2} H_n(t), \quad z_C = -\frac{1}{2} + \sum_{n=1}^{+\infty} \left[\frac{H_n(t)}{2}\right]^2,$$

while the mass center velocity is simply given by the time derivative of the mass center position, i.e $\dot{x}_C = u_C$ and $\dot{z}_C = w_C$. At each time step we first integrate the continuity equation and find $\dot{H}_n$ for each n. Then, we use these solutions to update the mass center velocity, compute f_1 and f_3 and, finally, integrate the momentum equation.

2.1   Global forces and moment on the tank

Here we derive the formulas for the generalized forces (namely, the mass forces and their moment with respect to a chosen point) on the tank per unit of breadth. All the details of computation can be found in the appendix A. Incidentally, we stress that the evaluation of the pressure distribution along the tank profile is far from being an easy task in the context of depth-averaged models. In fact, the pressure filed is not a principal variable of such schemes while it is generally expressed in terms of the depth-averaged velocity field, the instantaneous free-surface elevation and their derivatives. This makes the attainment of accurate results rather difficult. The expression for the pressure field is obtained from the work of Antuono and Brocchini (2013) and reads:

$$p = \left(\eta - \frac{z}{\epsilon}\right) + \mu^2 \frac{U_{xt}}{2} (\epsilon \eta - z)(\epsilon \eta - z - 2h) + \mu^2 T_w + \mathcal{O}\left(\epsilon \mu^2, \mu^4\right), \qquad (8)$$

where $p = p^*/(\rho^* g^* e_0^*)$ and

$$T_w = \sum_n^\infty n\pi \cos(n k x) \sum_m^\infty (m\chi)^{-3} \dot{\phi}_{n,m} \left[\cos(m\pi y) - 1\right]. \qquad (9)$$

The first term of the right-hand side of equation (8) represents the hydrostatic pressure while the remaining ones are the dynamic contributions from the laminar and turbulent motions respectively. The global forces on the tank (per unit of breadth) is given by:

$$\boldsymbol{F} = \int_{\partial \Omega_S} p \, \boldsymbol{n} \, dS, \qquad (10)$$

where Ω_S indicates the solid boundaries and $\boldsymbol{n}$ is the normal to $\partial \Omega_S$ pointing out of the fluid domain. We scale the components of $\boldsymbol{f}$ as follows:

$$F_1^* = \rho^* g^* e_0^* \, (h_0^* \, D^*) \, F_1 \qquad F_2^* = \rho^* g^* e_0^* \, (L^* \, h_0^*) \, F_2 \qquad F_3^* = \rho^* g^* e_0^* \, (L^* \, D^*) \, F_3.$$

In particular, we obtain the following formula for the x-component:

$$F_1 = \frac{\left(d_R^2 - d_L^2\right)}{2\,\epsilon} - \mu^2 \frac{h^3}{3} \sum_n^\infty n\pi \left[\left(\frac{d_R}{h}\right)(-1)^n - \left(\frac{d_L}{h}\right)\right] \dot{U}_n +$$

$$-\mu^2 h \sum_n^\infty n\pi \left[\left(\frac{d_R}{h}\right)(-1)^n - \left(\frac{d_L}{h}\right)\right] \sum_m^\infty (m\chi)^{-3} \dot{\phi}_{n,m}. \qquad (11)$$

where $d_R = (\epsilon \eta_R + h)$, $d_L = (\epsilon \eta_L + h)$ and:

$$\eta_L = \eta\big|_{x=0} = \sum_n^\infty H_n, \qquad \eta_R = \eta\big|_{x=1} = \sum_n^\infty (-1)^n H_n. \qquad (12)$$

Conversely, $F_2 = 0$ (no motion in the transverse direction) and $F_3 = -1/\epsilon$ (that is, only the hydrostatic component appears at the considered order of accuracy).

The global moment of the tank with respect to a chosen point $\boldsymbol{r_0} = (x_0, y_0, z_0)$ is:

$$\boldsymbol{M_0} = \int_{\partial \Omega_S} \left[(\boldsymbol{r} - \boldsymbol{r_0}) \times \boldsymbol{n}\right] p \, dS = \left[M_0^{(b)} + \mu^2 M_0^{(w)}\right] \boldsymbol{e_2}, \qquad (13)$$

8

where $\boldsymbol{e_2}$ is the unit vector in the transverse direction while the superscripts 'b' and 'w' denote the contributions coming from the integration along the bottom and along the vertical walls respectively. The scale for the moment $\boldsymbol{M}_0$ is set equal to $\rho^* g^* e_0^* D^* (L^*)^2$. After lengthy calculations (see the Appendix A.2), we find:

$$M_0^{(b)} = \frac{1}{\epsilon}\left(\frac{1}{2} - x_0\right) - \sum_{n=1}^{+\infty} \frac{[1 - (-1)^n]}{(n\,\pi)^2}\, H_n \;+\; \mu^2\, \frac{h^2}{2} \sum_{n=1}^{+\infty} \frac{[1 - (-1)^n]}{n\,\pi}\, \dot{U}_n$$

$$+ \mu^2 \sum_{n=1}^{+\infty} \frac{[1 - (-1)^n]}{n\,\pi} \sum_{m=1}^{+\infty} (m\chi)^{-3}\, [1 - (-1)^m]\, \dot{\phi}_{n,m}\,, \tag{14}$$

and

$$M_0^{(w)} = -z_0\, F_1 \;+\; \frac{h^2}{2} \sum_{n=1}^{+\infty} [1 - (-1)^n]\, H_n \;-\; \mu^2\, \frac{5}{24}\, h^4 \sum_{n=1}^{+\infty} n\,\pi\, [1 - (-1)^n]\, \dot{U}_n$$

$$- \mu^2\, \frac{h^2}{2} \sum_{n=1}^{+\infty} n\,\pi\, [1 - (-1)^n] \sum_{m=1}^{+\infty} (m\chi)^{-3}\, [1 - (-1)^m]\, \dot{\phi}_{n,m}$$

$$- \mu^2 \sum_{n=1}^{+\infty} n\,\pi\, [1 - (-1)^n] \sum_{m=1}^{+\infty} (m\chi)^{-5}\, [1 - (-1)^m]\, \dot{\phi}_{n,m}\,.$$

The coordinate in the transverse direction, namely y_0, gives no contribution to the global moment.

Note that the expression (13) states that the main contribution to the global moment comes from the bottom and that the action of horizontal component of the global force on $\boldsymbol{M}_0$ is weak, namely of order $\mathcal{O}\left(\mu^2\right)$. For the ease of the notation, hereinafter we write $\boldsymbol{M}_0 = M_2\, \boldsymbol{e_2}$, where M_2 is the overall contribution (from the walls and bottom) in the y-direction.

2.2 The sloshing model with diffusion

In Antuono et al. (2014) the above model has been successfully applied to a variety of practical sloshing phenomena, proving to be robust, accurate and reliable. Despite this, its range of application is limited to moderate breaking events. The main issue related to the occurrence of violent breaking waves is due to the incapability of the model to dissipate energy which, unavoidably, moves towards the higher modes generating spurious high frequency oscillations. It is worth noting that the use of a larger turbulent viscosity does not eliminate this problem. An alternative approach is to add a numerical diffusive term in the continuity equation in analogy to the linear term $\beta_n U_n$ in the momentum equation (which

is, however, motivated by an approximation of the dissipation induced by the boundary layer). The above idea is not new and has been applied, for example, in Molteni and Colagrossi (2009); Antuono et al. (2010, 2012b) in the framework of the Smoothed Particle Hydrodynamics (SPH), leading to stable and accurate schemes. More recently, a physical interpretation of the presence of the diffusive term in the continuity equation has been proposed in Di Mascio et al. (2017), where a Lagrangian LES-SPH scheme is derived. In sections 2.2.2 and 2.2.1 we better motivate the use of such a diffusive term and explain why its action is more effective in comparison to an increase of the turbulent viscosity. The continuity equation for the diffusive model reads:

$$\eta_t + (dU)_x - \delta_T\,\eta_{xx} = 0\,,\tag{15}$$

where δ_T is the diffusive parameter. In dimensional variables it has the dimensions of a kinematic viscosity. i.e. $\delta_T^* = \delta_0^*\,\delta_T$ where $\delta_0^* = L^*\sqrt{g^*\,h_0^*}$. Since the addition of the diffusive term is aimed at the modelling of violent breaking events, the coefficient δ_T is turn on just when wave breaking occurs, otherwise it is set to zero. The use of equation (15) modifies the first equation of the modal system as below:

$$\dot{H}_n + n\,\pi\,h\,U_n + \epsilon\,\frac{n\pi}{4}\sum_{p\in\mathbb{Z}}\Big[\,H_p\,U_{n-p} + H_{n-p}\,U_p\,\Big] + \delta_T\,n^2\pi^2\,H_n = 0\,.\tag{16}$$

Note that the use of the diffusive term does not compromise the mass conservation, since the mass flux at the tank walls is zero by construction (i.e. $\eta_x = 0$ at the walls).

Incidentally, we highlight that a further problem caused by the the generation of spurious oscillations concerns the identification of the point of the incipient wave breaking. Indeed, as described in Antuono et al. (2014), such a point is identified through the use of the x-derivative of the free-surface signal, namely η_x. Unfortunately, this quantity is much more noisy than η and a direct use of η_x generally leads to the identification of several spurious breaking points. This issue was already observed in Antuono et al. (2014) for weaker sloshing phenomena and it was overcome by using a smoothed free-surface signal. Unfortunately, for violent motions the smoothed datum may be very different from the original one, this leading to an erroneous identification of the position of the wave breaking. Remarkably, the use of a diffusive term *inside* the modal system completely remove this issue, since the free surface signal is sufficiently smooth and the breaking point can be identified by using η_x directly, without any external smoothing procedure.

2.2.1   *Physical interpretation of the diffusive term: a conjecture*

As shown in Antuono and Brocchini (2013), the system (1) is obtained by integrating the Reynolds equations over the water depth. These equations are

10

derived by applying the so-called Reynolds decomposition and an ensemble averaging procedure to the Navier-Stokes equations for *incompressible* flows. Under this hypothesis, the structure of the continuity equation stands unaltered and applies to both the averaged velocity field and its turbulent deviation. What we want to show is that this approach may be conceptually and physically imprecise since the incompressibility assumption is imposed too early in the derivation of the equations. Below, we propose an alternative approach that may be regarded as a weak formulation of the incompressibility assumption usually adopted in the scientific literature. Specifically, we start on the hypothesis that the fluid is compressible and, then, assume that the *averaged* fluid field is incompressible (while its deviation is not). This implies that an additional turbulent term should be included in the averaged continuity equation. This term may be modelled as a diffusive/dissipative term and may justify the use of equation (15).

Let us consider the continuity equation for a *compressible* fluid:

$$\rho_t + \nabla \cdot (\rho\, \boldsymbol{u}) = 0, \tag{17}$$

where ρ indicates the fluid density, $\boldsymbol{u} = (u, v, w)$ is the fluid velocity. Assuming the flow regime to be turbulent and averaging, we obtain:

$$\overline{\rho}_t + \nabla \cdot (\overline{\rho}\, \overline{\boldsymbol{u}}) + \nabla \cdot \langle \tilde{\rho}\, \tilde{\boldsymbol{u}} \rangle = 0, \tag{18}$$

where the overbarred variables are the Reynolds averaged variables, the symbol tilde indicates the turbulent deviations and the brackets $\langle \cdot \rangle$ indicate the Reynolds average. Now, we assume that the mean density field $\overline{\rho}$ has negligible variations (both in space and time) and that it can be approximated by a constant field $\overline{\rho}_0$. As a consequence, the continuity equation may be rewritten as follows:

$$\nabla \cdot \overline{\boldsymbol{u}} + \nabla \cdot \langle \tilde{\varrho}\, \tilde{\boldsymbol{u}} \rangle = 0, \tag{19}$$

where $\tilde{\varrho} = \tilde{\rho}/\overline{\rho}_0$. Note that, with respect to the usual approach, we relaxed the incompressibility assumption since we assumed that only the *averaged* field is incompressible while its deviation is not. Integrating the equation (19) over the fluid depth with the usual boundary conditions (see Antuono and Brocchini 2013 for details), we obtain:

$$\eta_t + \hat{\nabla} \cdot (d\boldsymbol{U}) + \int_{-h}^{\epsilon\eta} \nabla \cdot \langle \tilde{\varrho}\, \tilde{\boldsymbol{u}} \rangle \, \mathrm{d}z = 0, \tag{20}$$

where $\hat{\nabla} = (\partial/\partial x, \partial/\partial y)$ is the gradient over the (x, y)-plane and $\boldsymbol{U}$ is the depth-averaged velocity. Using the Leibniz rule and neglecting the turbulent stresses along the free surface and the bottom (this is a standard hypothesis for depth-averaged equations, e.g. Antuono and Brocchini 2013), we rearrange the last term as follows:

11

$$\eta_t + \hat{\nabla} \cdot (d\boldsymbol{U}) + \hat{\nabla} \cdot \boldsymbol{S} = 0, \tag{21}$$

where

$$\boldsymbol{S} = \left(\int_{-h}^{\epsilon\eta} \langle \tilde{\varrho}\,\tilde{u} \rangle \,\mathrm{d}z, \int_{-h}^{\epsilon\eta} \langle \tilde{\varrho}\,\tilde{v} \rangle \,\mathrm{d}z \right). \tag{22}$$

Following a Fickesian approach, we may assume the above term to be proportional to the gradient of η, thus motivating the use of equation (15).

Assuming $|\tilde{\varrho}| \ll 1$, the same approach leads to the following additional terms in the averaged momentum equation:

$$\left\langle \frac{\nabla p}{\rho} \right\rangle = \frac{\nabla \overline{p}}{\overline{\rho}_0} \left(1 + \langle \tilde{\varrho}^2 \rangle \right) - \frac{\langle \tilde{\varrho}\,\nabla \tilde{p} \rangle}{\overline{\rho}_0} + \dots \tag{23}$$

In any case, because of the assumption on $|\tilde{\varrho}|$, these terms may be regarded as negligible in comparison with the Reynolds stresses.

2.2.2 Dispersion, non-linearities and diffusion

It is worth noting that the occurrence of spurious high frequency oscillations for strong sloshing phenomena mainly affects the signal of the free-surface elevation while the velocity field is generally more regular. This is caused by three interacting phenomena: *i)* the reduction of the kinetic energy flux towards the higher modes due to the dispersion, *ii)* the different ways in which the energy is redistributed over the modes by the non-linear terms of the continuity and momentum equations, *iii)* the absence of dissipative/diffusive terms in the continuity equation.

To better explain the above points, we consider the equations of the potential (elastic) energy and of the kinetic energy. These are obtained by multiplying the first equation of the modal system (without diffusion) by H_n and the momentum equation by U_n. The equation for the elastic energy of the n-th mode reads:

$$\frac{\mathrm{d}}{\mathrm{d}t}\left(\frac{H_n^2}{2} \right) + n\,\pi\,h\,H_n\,U_n + \epsilon\,\frac{n\pi H_n}{4} \sum_{p\in\mathbb{Z}} \left[H_p\,U_{n-p} + H_{n-p}\,U_p \right] = 0, \tag{24}$$

while the kinetic energy equation is:

$$\alpha_n \frac{\mathrm{d}}{\mathrm{d}t}\left(\frac{U_n^2}{2} \right) + n\pi f_3 H_n U_n + \beta_n U_n^2 + \epsilon\frac{n\pi U_n}{4} \sum_{p\in\mathbb{Z}} U_p U_{n-p} + W_n U_n = \frac{f_1}{\mu}\gamma_n U_n, \tag{25}$$

12

where $\alpha_n = (1 + \mu^2 n^2 \pi^2 h^2/3)$ and W_n includes all the remaining terms (i.e. the turbulent and vortical contributions). The point i) is strictly related to the action of the coefficient α_n, this accounting for the dispersive effects. Indeed, dividing equation (25) by α_n, it appears clear that the dispersion acts in opposition to the non-linear terms reducing the kinetic energy of the higher modes.

For what concerns the point ii), we first observe that the summation all over the modes of the non-linear term in equation (25) is null, that is (see the appendix B for details):

$$\sum_{n \in \mathbb{Z}} n\, U_n \sum_{p \in \mathbb{Z}} U_p U_{n-p} = 0\,. \tag{26}$$

Remarkably, the above relations still hold true in the presence of a finite number of modes. This result proves that the non-linear term in the momentum equation just redistributes the kinetic energy all over the modes (specifically, towards the higher modes) without affecting its total amount. On the contrary, the summation all over the modes of the non-linear term in equation (24) is generally different from zero. Consequently, such a non-linear term may be regarded as a source/sink term in the potential energy equation fed by the velocity field. Differently from the kinetic energy equation, the absence of any diffusive/dissipative term cannot reduce the energy flux towards the higher modes, this process being even stronger when a finite number of modes is considered. This explains the excess of larger spurious frequencies in the free-surface signal when strong non-linear sloshing phenomena are modelled and motivates the use of a numerical diffusive term in the continuity equation.

2.2.3   Preliminary application of the diffusive model

In the present section we briefly consider some applications of the diffusive model to some problems already discussed in Antuono et al. (2014). The aim is to briefly show how the use of the diffusion influences the dynamics of sloshing phenomena characterized by weakly-breaking waves and to highlight when it is helpful for the numerical modelling. The order of magnitude of the diffusive coefficient is chosen to be $\mathcal{O}(10^{-3})$, so that its action becomes non-negligible just for $n \geq 10$. Specifically, we set $\delta_T = 0.002$ in all the simulations presented in this work. Minor variations of the results are observed for small variations of δ_T around the above value.

We consider two sway motions described in Antuono et al. (2014) (the tank dimensions are $L^* = 1m$, $D^* = 0.1m$) which are both characterized by plunging breaking events. In the first case, the filling height is $h^* = 0.125$ (almost intermediate regime) and the corresponding first resonant frequency is $\sigma_r^* = 3.3936\,rad/s$. The forcing excitation for this motion is given by:
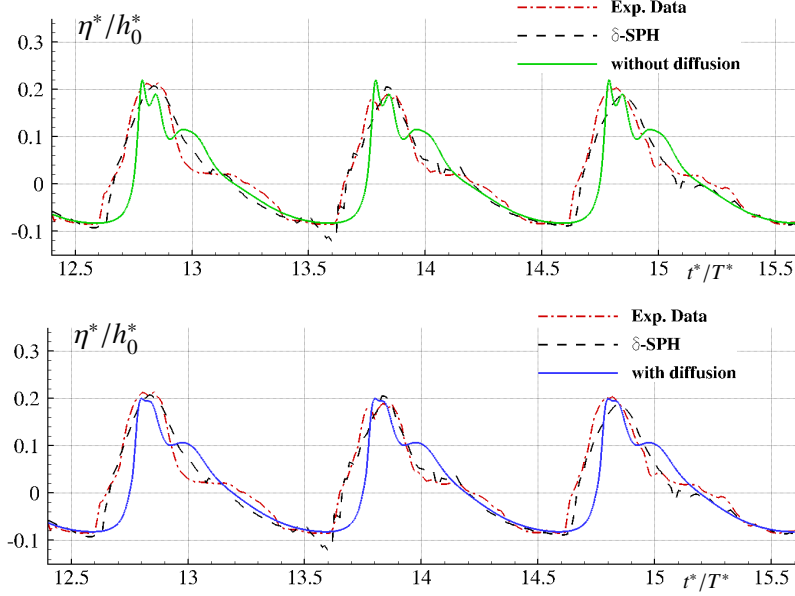
Fig. 2. Free-surface elevation at $x^*/L^* = 0.05$ for the sloshing case denoted "Series 2" described in Antuono et al. (2014). Comparison with the δ-SPH scheme of Antuono et al. (2010) and with the experimental data. Solid lines indicate the modal scheme with (bottom) and without (top) diffusion while numerical and experimantal signals are the same in both panels.

$$ x^*_{0,1} = A^*_{0,1} \sin(\sigma^* t^*) , \quad \Rightarrow \quad a^*_{0,1} = \ddot{x}^*_{0,1} = -(\sigma^*)^2 A^*_{0,1} \sin(\sigma^* t^*) , \quad (27) $$

where $A^*_{0,1} = 0.1m$ and $\sigma^*/\sigma^*_r = 1$ while the reference period is $T^* = 2\pi/\sigma^*$. The top panel of Figure 2 shows the comparison of the model without diffusion (i.e. $\delta_T = 0$) with the δ-SPH and the experimental measurements for the free-surface elevation at $x^*/L^* = 0.05$. The same numerical and experimental data are displayed in the bottom panel of the same figure along with the proposed diffusive scheme. In this case the diffusive model predicts a slightly smoother profile than the model without diffusion but the signals are practical identical and are both in good agreement with experiments and numerics. This confirms that the action of diffusion plays a minor role when the basic model (that is the model with $\delta_T = 0$) works properly.

On the contrary, the use of a diffusive scheme becomes crucial in some sloshing cases where the scheme without diffusion reveals inaccurate. An example is shown in figure 3 where the so-called "Series 3" described in Antuono et al. (2014) is considered. This case is characterized by a shallow filling depth, i.e. $h^* = 0.03$, and is very close to the bifurcation ($\sigma^*/\sigma^*_r = 1.230$, $A^*_{0,1} = 0.07m$). Both numerical and experimental data are compared to the model without diffusion in the top panel of figure 3 and to the proposed diffusive variant in the bottom panel of the same figure. In the case without diffusion, the small filling heigh ($h^*/L^* = 0.03$) leads to the generation of a sort of undular bore that travels back and forth the tank. This phenomenon is likely caused by an incorrect interaction between the dispersive term in the momentum equation and the nonlinear terms. It generally occurs when
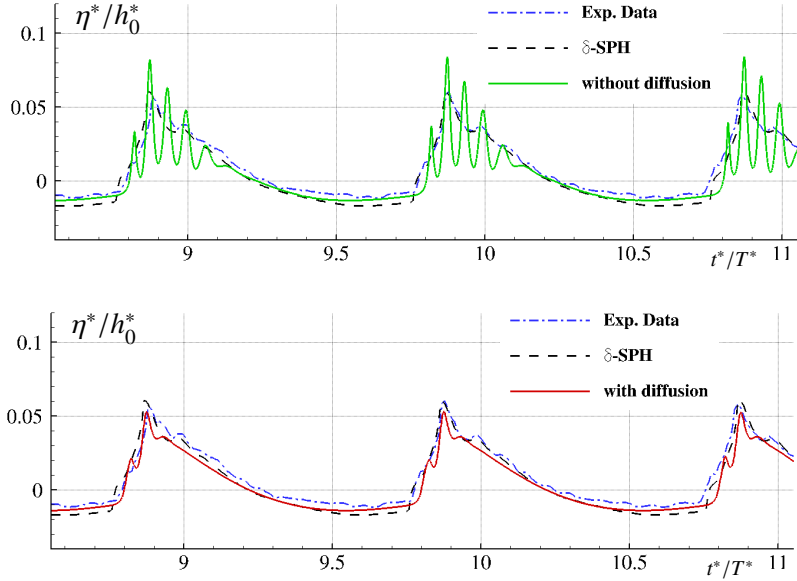
14

Fig. 3. Free-surface elevation at $x^*/L^* = 0.05$ for the sloshing case denoted "Series 3" with $\sigma^*/\sigma_r^* = 1.230$ described in Antuono et al. (2014). Comparison with the δ-SPH scheme of Antuono et al. (2010) and with the experimental data. Solid lines indicate the modal scheme with (bottom) and without (top) diffusion while numerical and experimantal signals are the same in both panels.

the wave front is sharp (for example, in the presence of a travelling bore) and the wave is advancing in very shallow depths. As shown in the bottom panel of figure 3, the use of diffusion helps eliminating this issue (the signal of the diffusive model is free from oscillations and appears in very good agreement with both experiments and numerics), since it breaks the interaction between the dispersive term in the momentum equation and the nonlinear term in the continuity equation.

For the time being, we can state that the use of the diffusive model may cause a slight damping of the weaker sloshing motions but, in turn, it may be a reliable tool for a correct modelling of strong phenomena, especially in shallow water conditions. All these aspects will be analysed more in depth in the following Sections, highlighting the main advantages/drawback of the proposed scheme.

3 Applications

In the present section we show various applications to sloshing phenomena of practical interest. In particular, we consider roll motions described by the following law:

$$\theta = \theta_0 \sin(\sigma^* t^*), \tag{28}$$

15
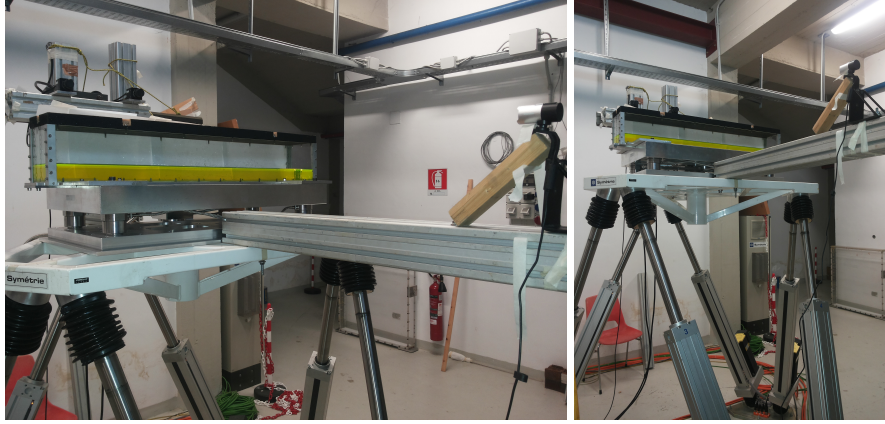
Fig. 4. The experimental set-up.

at increasing angles of excitation, namely $\theta_0 = 2°, 4°, 6°$, and at different excitation frequencies (the values for σ^* are reported in Table 1 and the reference period is $T^* = 2\pi/\sigma^*$). These cases represent very challenging problems since they are characterized by strong breaking events and, in some configurations, by the occurrence of almost dry conditions along the tank bottom. Under these conditions, the use of the diffusive scheme is of great importance for the stability of the modal scheme and for an accurate description of the physical phenomenon. All the simulations that follow have been implemented by using 200 modes in the x-direction and 50 along the vertical direction.

3.1 Experimental setup

The experiments have been performed at the CNR-INSEAN Sloshing Lab. A 6DOF mechanical system Mistral by Symetrie has been used to force the tank motion; it ensures an accuracy of 0.2 deg for the angular and 1 mm for the linear displacements. The tank is $L^* = 0.94$ m long, $D^* = 0.13$ m wide and is filled with water up to a height $h^* = 0.04$ m (see sketch of figure 1), that is the lowest natural frequency is equal to $\sigma_r^* = 2.0874 \, rad/s$. The narrow tank, *i.e.* $D^*/L^* = 0.1383$, ensures an almost-2D flow in the main tank plane. The axis of rotation is set at a distance of 0.41 m below the center of the tank bottom.

Present experimental activity is part of the Project *NSCS* which aims at the estimation of the roll damping induced by an antirolling tank on a fishing vessel. To the purpose a suitable balance has been designed and built at CNR-INSEAN to measure the forces and moments induced by the free-surface tank. The balance uses a Kistler 9366CC multicomponent force link kit, composed by four 3-component piezo-electric force sensors. A rigid top plate in aluminium is used to transfer the load to the force sensors; the chosen thickness ensures a structural natural frequency around 600 Hz. The piezo-electric technology ensures the measurement without any displacement. From the measurement of the forces by the four 3-

θ_0	σ^*/σ_r^*			
2°	\	0.7736	1.0027	1.2377
4°	0.4641	0.7736	1.0027	\
6°	\	0.7736	1.0027	\

Table 1

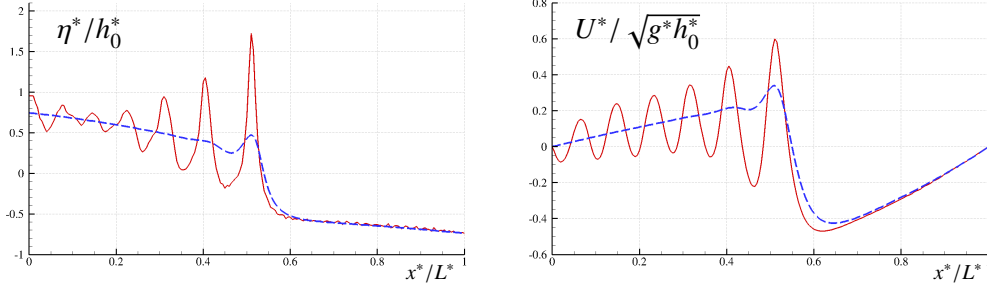The experimental campaign considered in the present work.

Fig. 5. snapshot of the free-surface elevation (left) and of the velocity field (right) as predicted by the modal method with (dashed lines) and without (solid lines) diffusion for $\theta_0 = 2°$ and $\sigma^*/\sigma_r^* = 0.7736$.

component cells it is possible to determine the global forces and moments. The whole balance has been calibrated by the certified Kistler calibration laboratory. A maximum linearity error less than 0.1% FSO (Full Scale Output) and a cross-talk error less than 1% FSO has been certified along each measurement axis, for a value of FSO= $0.3kN$.

The experimental set-up is shown in figure 4. Beyond the balance a standard low resolution digital camera (30 frame per second, $640x480$ pixels, 24 bit) has been used to record the free-surface motion in a reference system fixed to the tank. An acquisition system Prosig P8048 enables the recording of the generalized forces and tank motion at a sample freqeuncy of 1000 Hz. A suitable trigger signal is used to synchronize the camera with the acquisition system and the motion of the mechanical system.

3.2   Roll motion at 2 degrees

For $\theta_0 = 2°$, three cases have been considered, namely $\sigma^*/\sigma_r^* = 0.7736$, 1.0027, 1.2377 (see Table 1). The first two cases are characterized by spilling breaking events while a weak plunging breaking is observed for $\sigma^*/\sigma_r^* = 1.2377$.

Before proceeding to the comparison with the experiments, we briefly discuss the action of the proposed diffusive term. Figure 5 displays some snapshots of the free-surface elevation (left) and of the velocity field (right) as predicted by the modal method with and without diffusion (dashed and solid lines respectively) for $\sigma^*/\sigma_r^* = 0.7736$. Consistently with the results shown in the Section 2.2.3, the action
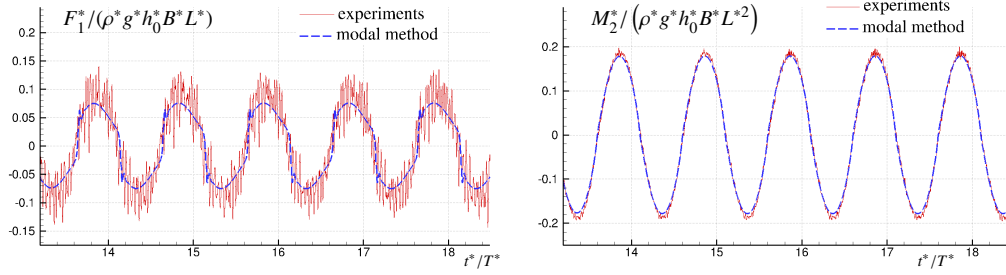
17

Fig. 6. global force (left) and moment (right) for $\theta_0 = 2°$ and $\sigma^*/\sigma_r^* = 0.7736$. Comparison between the experiments and the modal scheme with diffusion.

of the diffusion prevents the occurrence of large spurious oscillations in both the surface and velocity signals. Surprisingly, the improvements on the signals of the global force and moment are small in comparison with the non-diffusive model (which is, therefore, not shown in the present section). This behaviour is probably due to the weaker dynamics that characterizes the motions for $\theta_0 = 2°$ and/or to the cancellation of the oscillations that occurs during the computation of the global loads (that is, during the integration of the pressure field along the tank boundaries).

A further improvement related to the use of diffusion concerns the computational time. For 100 seconds of physical evolution over a single Xeon 2.33 GHz processor, the diffusive variant is about 5 times faster than the model without diffusion (specifically, about 6 minutes of computational time against 32 minutes). This is mainly due to the larger stability of the diffusive scheme that allows for an initial time step that is twice larger than the model with $\delta_T = 0$. In addition, the time step is modified dynamically by taking into account the time derivatives of the modes, that is $\dot{H}_n$ and $\dot{U}_n$ (namely, the accelerations of the modal scheme). Since the use of diffusion allows for smoother solutions and, therefore, for smaller time derivatives, the dynamical variations of the time step of the diffusive scheme are more restrained than the model without diffusion. Finally, the non-diffusive version is sometimes characterized by the identification of spurious breaking points, because of the numerical noise affecting the free-surface solution. This leads to additional computational costs in comparison to the diffusive scheme.

Figure 6 displays the numerical and experimental signals of force and moment for $\sigma^*/\sigma_r^* = 0.7736$. The experimental forces and moments show a quite evident high-frequency noise, which is related to the vibration of the hexapod mechanism. However, this frequency is well far from the forcing frequency of the motion as well as from the related sloshing frequencies. With the aim to avoid any alteration of the original data, we have chosen to show the experimental data at the original sample rate (i.e. 1 kHz) avoiding any filtering. In both the cases, an overall good match is observed. Note that the moment signal (right panel) is very close to a sinusoidal profile, this meaning that the influence of nonlinear contributions is small. Such a behaviour is rather different from that shown by the time history of the global force (left panel) which appears quite distorted. Incidentally, this confirms the observation carried out at the end of section 2.1 where a weak influence of the
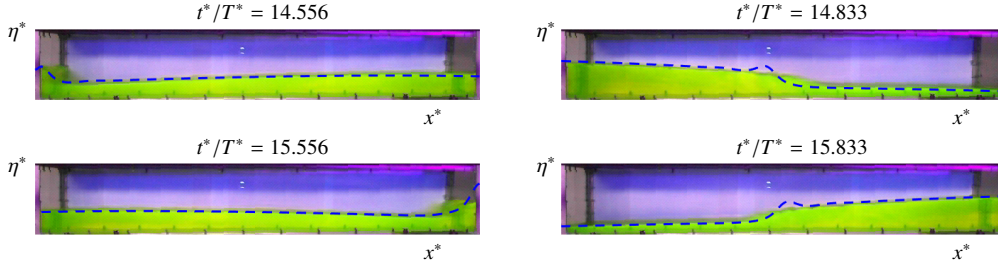
18

Fig. 7. Snapshots of the evolution for $\theta_0 = 2°$ and $\sigma^*/\sigma_r^* = 0.7736$ Comparison between the experiments and the numerical wave elevation (thick dashed lines) at different time instants.
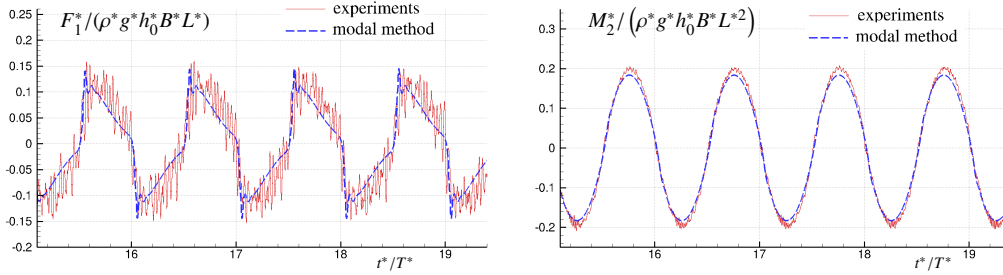

Fig. 8. global force (left) and moment (right) for $\theta_0 = 2°$ and $\sigma^*/\sigma_r^* = 1.0027$. Comparison between the experiments and the modal scheme with diffusion.

horizontal component of the global force on the moment is underlined.

Figure 7 shows some snapshots of the sloshing dynamics at different time instants along with the numerical solution of the free-surface elevation (dashed lines). The agreement between the numerical and experimental wave elevation is fairly good, except for the wave front where the numerical signal predicts a bump-like profile while the experiments show a more rounded shape. For shallow water problems (like the cases discussed in the present work), this is typical limit of the modal scheme and is caused by the inaccurate modelling of the dispersive effects. As we show in the sequel, this issue is more and more evident as the dynamics becomes more violent.

For $\sigma^*/\sigma_r^* = 1.0027$, the roll motion is more severe and the nonlinearities of the force signal become more pronounced, showing a sawtooth profile (see the top panel of figure 8) while, the moment profile is still very regular. In any case, the agreement between experiments and the modal scheme is still very good.

Finally, figure 9 displays the most violent roll motion for $\theta_0 = 2°$, namely $\sigma^*/\sigma_r^* = 1.2377$. Both the time histories of the force and the moment are quite similar to the previous case even though the amplitude of the moment signal under-predicts the experimental measurements of about 20%. Apart from this, the overall agreement maintains fairly good.
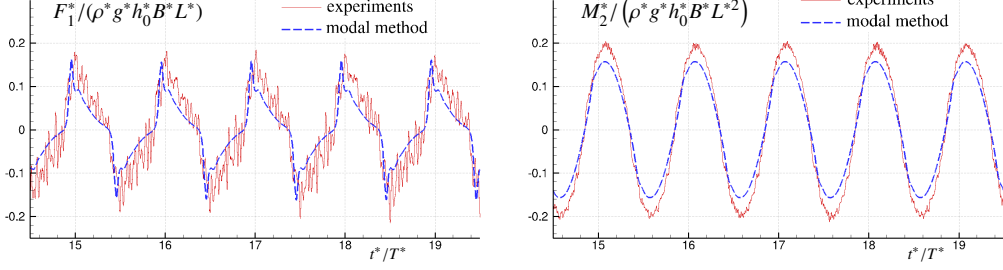
19

Fig. 9. global force (left) and moment (right) for $\theta_0 = 2°$ and $\sigma^*/\sigma_r^* = 1.2377$. Comparison between the experiments and the modal scheme with diffusion.
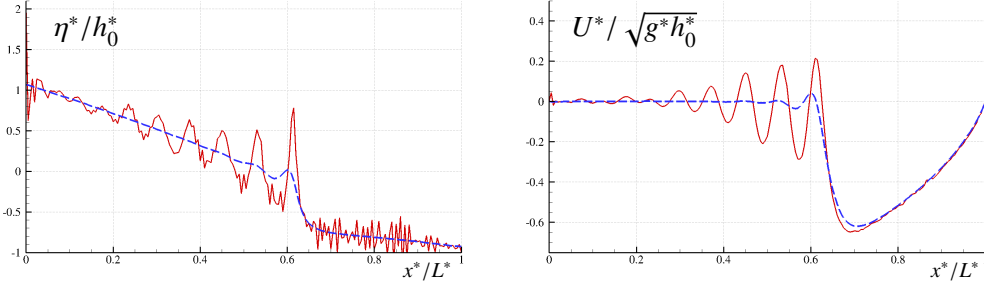

Fig. 10. snapshot of the free-surface elevation (left) and of the velocity field (right) as predicted by the modal method with (dashed lines) and without (solid lines) diffusion for $\theta_0 = 4°$ and $\sigma^*/\sigma_r^* = 0.4641$.

3.3 Roll motion at 4 degrees

For $\theta_0 = 4°$ we consider three roll cases (see Table 1) characterized by rather different behaviours. For $\sigma^*/\sigma_r^* = 0.4641$ the wave motion is weak with small spilling waves and almost dry conditions at the front of the leading edge. The latter one is a challenging configuration for the modal scheme, since the dispersive effects are roughly represented and tend to generate large spurious oscillations while, on the other hand, the nonlinearities are strong and play a relevant role in the leading edge dynamics. Figure 10 displays a comparison between the modal scheme with and without diffusion for the free-surface and velocity signals. In addition to the large oscillations due to the inaccurate modelling of the dispersive effects, the free surface of the model without diffusion is also affected by high-frequency noise caused by the nonlinearities and by the related energy flux towards the higher modes (see the discussion in section 2.2.2). It is worth noting that the velocity profile of the model without diffusion is much more regular than the free-surface signal. As explained in section 2.2.2, this is due to the action of the damping terms in the momentum equation which play in opposition to the nonlinear effects, limiting the energy flux towards the higher modes. In both the cases, the diffusive scheme gives regular profiles for both the velocity and the free surface.

Figure 11 shows the comparison between the measurements of the global force and the sloshing model with and without diffusion (left and middle panels respectively).
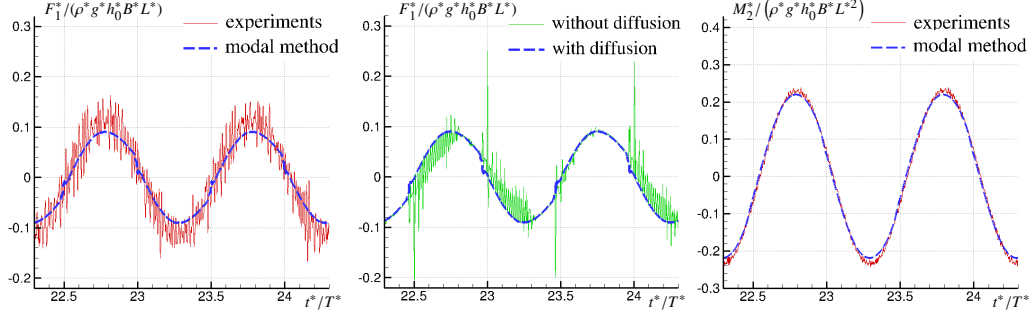
20

Fig. 11. global force (left and middle panels) and moment (right panel) for $\theta_0 = 4°$ and $\sigma^*/\sigma_r^* = 0.4641$. Left and right panels: comparison between the experiments and the modal scheme with diffusion. Middle: comparison between the modal scheme with and without diffusion.
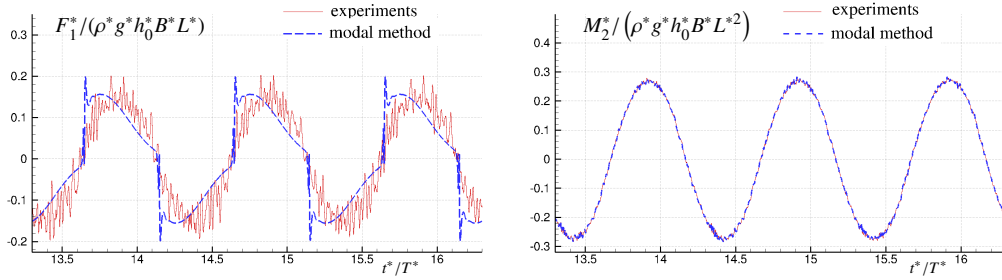

Fig. 12. global force (left) and moment (right) for $\theta_0 = 4°$ and $\sigma^*/\sigma_r^* = 0.7736$. Comparison between the experiments and the modal scheme with diffusion.

In the latter case, the spurious noise affects the prediction of the global loads on the tank, further confirming the reliability and accuracy of the diffusive approach. For what concerns the prediction of the global moment, the differences between the scheme with and without diffusion are small and, therefore, only the former model is shown in the sequel. The moment signal is drawn in the right panel of figure 11, providing a good match between numerics and experiments.

The second roll case (namely $\sigma^*/\sigma_r^* = 0.7736$) is characterized by a stronger dynamics, with moderate spilling breaking events and, similarly to the previous case, with almost dry conditions at front of the leading edge. The comparisons between the measured values of the global force and moment and the corresponding numerical outputs are displayed in Figure 12. The agreement for the moment is excellent while the force signal is rather different from the measurements, even though its magnitude is correctly predicted. The above discrepancy is caused by the different profile of the wave front with respect to the experiments (see the snapshots of the evolution in figure 13). The bump-like profile of the numerical wave front is somehow similar to that described in figure 7 for $\theta_0 = 2°$, even if a worse behaviour is observed in the present case because of a more violent dynamics. As already pointed out, the different shape of the wave front between the numerical outputs and the experiments does not affect the moment signal. This is probably due to the weak dependence of the moment on the nonlinearities.
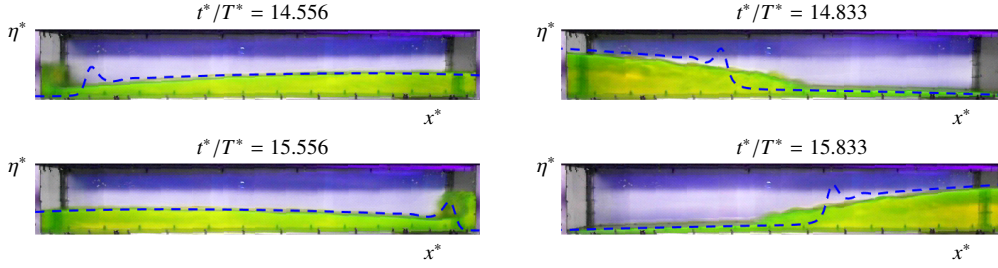
Fig. 13. Snapshots of the evolution for $\theta_0 = 4°$ and $\sigma^*/\sigma_r^* = 0.7736$. Top panels: comparison between the experiments and the numerical wave elevation (thick dashed lines). Middle and bottom panels: time histories of the experimental and numerical moment and force (the vertical dashed lines indicate the time instant of the corresponding snapshots).
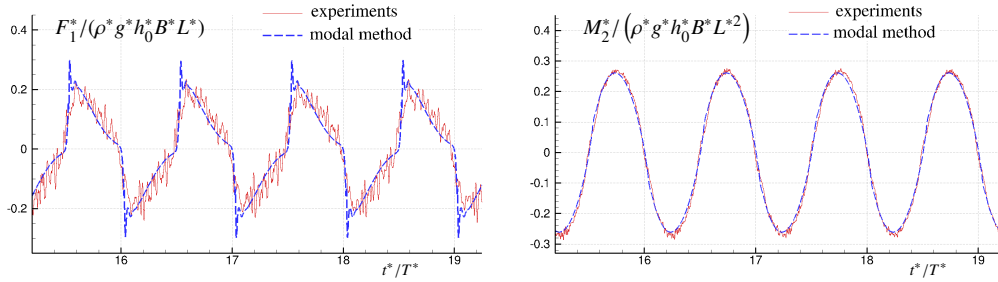

Fig. 14. global force (left) and moment (right) for $\theta_0 = 4°$ and $\sigma^*/\sigma_r^* = 1.0027$. Comparison between the experiments and the modal scheme with diffusion.

For what concerns the roll case with $\sigma^*/\sigma_r^* = 1.0027$, the shape of the force signal shows a more satisfying agreement with the experiments (left panel of figure 14), even though the peaks of the numerical solution overestimate the experimental datum of about 40%. This latter behaviour is a consequence of the rather violent dynamics and of the occurrence of plunging breaking waves during the evolution. In turn, the water depth at the leading edge is less shallow than the previous roll simulations and this explains the improvement in the shape of the force signal. As usual, the moment is in very good agreement with the experimental measurements (see the right panel of figure 14).

3.4   Roll motion at 6 degrees

The last part of the analysis is devoted to the roll tests at $\theta_0 = 6°$ (see table 1). These motions are all characterized by strong plunging waves at the tank sides and by almost dry conditions at the leading edge of the wave front. In this case, the model without diffusion is not stable and the simulations can be achieved only by using the diffusive scheme.

Figure 15 displays the comparisons between the numerical solution and experimental measurements for the global force and moment for $\sigma^*/\sigma_r^* = 0.7736$. Similarly to the roll cases at $\theta_0 = 2°$ and $\theta_0 = 4°$, the moment is correctly predicted by the diffusive model while, on the contrary, the force is rather different
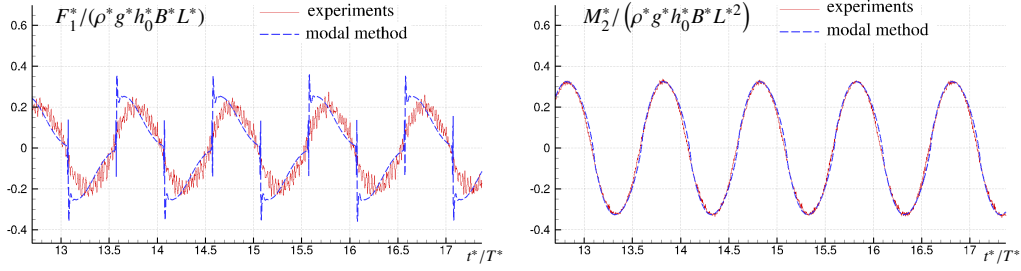
Fig. 15. global force (left) and moment (right) for $\theta_0 = 6°$ and $\sigma^*/\sigma_r^* = 0.7736$. Comparison between the experiments and the modal scheme with diffusion.

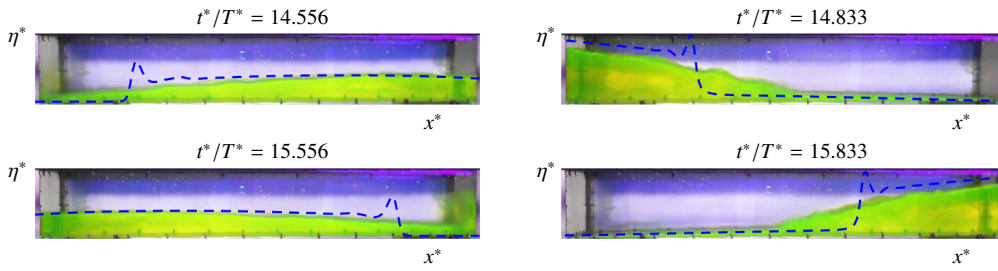

Fig. 16. Snapshots of the evolution for $\theta_0 = 6°$ and $\sigma^*/\sigma_r^* = 0.7736$. Top panels: comparison between the experiments and the numerical wave elevation (thick dashed lines). Middle and bottom panels: time histories of the experimental and numerical moment and force (the vertical dashed lines indicate the time instant of the corresponding the snapshots).

from the experimental datum. In particular, the numerical solution is similar to the signal displayed in figure 12 (top panel) for $\theta_0 = 4°$, even if a sharper profile and a larger overestimation of the maximum peaks are observed. This behaviour is a consequence of the sharp wave front predicted by the numerical solution in comparison with the experiments (see the snapshots of the evolution in figure 16). As already discussed in the previous section, the occurrence of such a phenomenon is a consequence of an inaccurate modelling of the dispersive effects and of their interaction with nonlinearities when the fluid motion becomes very energetic and the wave depth is very shallow (i.e. almost dry conditions at the wave front).

As a confirmation of the above reasoning, we observe a slight improvement of shape of the force signal in comparison to the experiments for $\sigma^*/\sigma_r^* = 1.0027$ (see the left panel of figure 17). In fact, in this case the fluid dynamics is still violent but the water depth at the wave front is less shallow. Apart from this, the maximum value of the numerical force largely overestimates the experimental measurements. On the contrary, the agreement maintains good for the moment (see the right panel of 17).
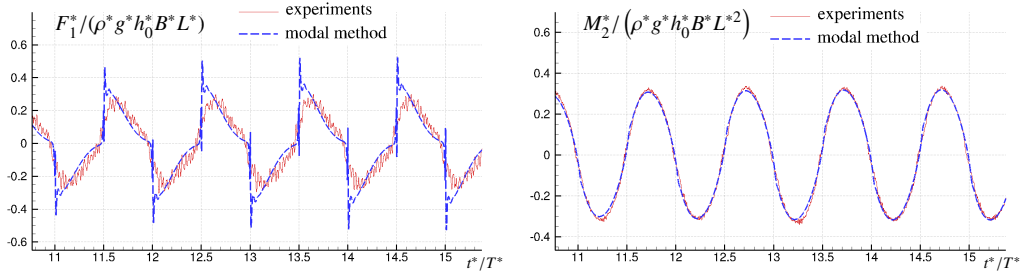
Fig. 17. global force (left) and moment (right) for $\theta_0 = 6°$ and $\sigma^*/\sigma_r^* = 1.0027$. Comparison between the experiments and the modal scheme with diffusion.

Conclusions

Basing on the modal representation of the sloshing motion in shallow water conditions introduced in Antuono et al. (2012a) and successively extended in Antuono et al. (2014), we derived the expressions for the global force and moment acting on a rectangular two-dimensional tank. Further, to overcome the limits of the modal scheme when the water depth is very shallow, a diffusive variant has been proposed, this relying on the use of a diffusive term in the continuity equation of the depth-averaged system in Antuono and Brocchini (2013). A qualitative description of the interaction between diffusion, dispersion and nonlinearities has been attempted, along with a possible physical interpretation of the diffusive term.

The numerical outputs have been extensively validated through comparison with experimental data for roll motions at different angles of excitement, namely $\theta_0 = 2°, 4°, 6°$. The overall fair agreement between the numerical solutions and the experiments confirms the accuracy of the model, even though some issues arise in the evaluation of the forces when the roll angle is large (namely, $\theta_0 = 6°$) and the wave front travels in almost dry conditions. Future studies will be dedicated to overcome the above limitations and increase the accuracy of the modal scheme.

A Details of computations

In the present section we show the details of computation of the global forces on the tank and of their moment with respect to a chosen point.

A.1 Global Forces

To compute the global forces (per unit of breadth) on the tank we need the expression for the pressure field. This is obtained from the work of Antuono and Brocchini (2013) and, at the desired order of accuracy, reads:

$$\frac{p^*}{\rho^*} = g^* (\eta^* - z^*) + \frac{U^*_{x^* t^*}}{2} (\eta^* - z^*) (\eta^* - z^* - 2 h^*) + T^*_w, \tag{A.1}$$

where

$$T^*_w = \sum_n n k^* \cos(n k^* x^*) \sum_m (m \chi^*)^{-3} \dot{\phi}^*_{n,m} \left[\cos(m \pi y) - 1 \right]. \tag{A.2}$$

Here, $\chi^* = \pi/h^*$ and $k^* = \pi/L^*$ while y is a dimensionless coordinate in the vertical direction:

$$y = - \left(\frac{\eta^* - z^*}{d^*} \right) \tag{A.3}$$

The global forces on the tank is given by:

$$\boldsymbol{F}^* = \int_{\partial \Omega_S} p^* \boldsymbol{n} \, dS^*, \tag{A.4}$$

where Ω_S indicates the solid boundaries. Specifically, the horizontal and vertical components (per unit of breadth) are:

$$\frac{F^*_1}{D^*} = \int_{-h^*}^{\eta^*_R} p^*|_{x^*=L^*} \, dz^* - \int_{-h^*}^{\eta^*_L} p^*|_{x^*=0} \, dz^*, \qquad \frac{F^*_3}{D^*} = \int_0^{L^*} p^*|_{z^*=-h^*} \, dx^*, \tag{A.5}$$

where D^* is the tank breadth and:

$$\eta^*_L = \eta^*\big|_{x^*=0} = \sum_n^{\infty} H^*_n, \qquad \eta^*_R = \eta^*\big|_{x^*=L^*} = \sum_n^{\infty} (-1)^n H^*_n. \tag{A.6}$$

25

At the current order of approximation, it is simple to prove that $F_3^* = -\rho^* g^* h^* D^* L^*$. This means that the leading order of the force along the bottom is due to the hydrostatic pressure. The evaluation of the horizontal component is a bit more laborious. We obtain:

$$\int_{-h^*}^{\eta_R^*} p^*|_{x^*=L^*}\, dz^* = \rho^* g^* \frac{(\eta_R^* + h^*)^2}{2} + \frac{\rho^*}{6} (\eta_R^* + h^*)(\eta_R^{*2} - \eta_R^* h^* - 2h^{*2})\, U_{x^*t^*}^{*R}$$

$$-\rho^*(\eta_R^* + h^*) \sum_n^\infty n\, k^*\, (-1)^n \sum_m^\infty (m\chi^*)^{-3} \dot{\phi}_{n,m}^*,$$

where $(\eta_R + h)$ is the total water depth at the right wall and:

$$U_{x^*t^*}^{*R} = U_{x^*t^*}^*\big|_{x^*=L^*} = \sum_n^\infty n\, k^* (-1)^n\, \dot{U}_n^*. \tag{A.7}$$

Similarly, we find:

$$\int_{-h^*}^{\eta_L^*} p^*|_{x^*=0}\, dz^* = \rho^* g^* \frac{(\eta_L^* + h^*)^2}{2} + \frac{\rho^*}{6} (\eta_L^* + h^*)(\eta_L^{*2} - \eta_L^* h^* - 2h^{*2})\, U_{x^*t^*}^{*L}$$

$$-\rho^*(\eta_L^* + h^*) \sum_n^\infty n\, k^* \sum_m^\infty (m\chi^*)^{-3} \dot{\phi}_{n,m}^*,$$

where:

$$U_{x^*t^*}^{*L} = U_{x^*t^*}^*\big|_{x^*=0} = \sum_n^\infty n\, k^*\, \dot{U}_n^*. \tag{A.8}$$

The final formula for the horizontal force is obtained by collecting together the above contributions and dropping the higher order terms. Incidentally, we underline that some terms of order $\mathcal{O}(\epsilon\mu^2)$ have to be retained since they provide the correct behaviour for shallow depths, that is for $(\eta_R^* + h^*)$ and/or $(\eta_L^* + h^*)$ going to zero. Specifically, we write:

$$F_1^* = \rho^* D^* \left\{ g^* \frac{\left(d_R^{*2} - d_L^{*2}\right)}{2} - \frac{h^{*3}}{3} \sum_n^\infty n\, k^* \left[\left(\frac{d_R^*}{h^*}\right)(-1)^n - \left(\frac{d_L^*}{h^*}\right) \right] \dot{U}_n^* + \right.$$

$$\left. -h^* \sum_n^\infty n\, k^* \left[\left(\frac{d_R^*}{h^*}\right)(-1)^n - \left(\frac{d_L^*}{h^*}\right) \right] \sum_m^\infty (m\chi^*)^{-3} \dot{\phi}_{n,m}^* \right\}.$$

where $d_R^* = (\eta_R^* + h^*)$ and $d_L^* = (\eta_L^* + h^*)$.

A.2 Global Moment

Here we compute the global moment of the tank with respect to a fixed point $\boldsymbol{r_0} = (x_0, y_0, z_0)$, that is:

$$\boldsymbol{M}_0^* = \int_{\partial \Omega_S} \left[(\boldsymbol{r}^* - \boldsymbol{r}_0^*) \times \boldsymbol{n} \right] p^* \, dS^* . \tag{A.9}$$

The component along the bottom (per unit of breadth) is:

$$\frac{\boldsymbol{M}_B^*}{D^*} = - \int_0^{L^*} \left[(\boldsymbol{r}^* - \boldsymbol{r}_0^*) \times \boldsymbol{e_3} \right] \left. p^* \right|_{z^* = -h^*} dx^* , \tag{A.10}$$

where $\boldsymbol{r}^* = (x^*, y_0^*, -h^*)$. Expanding the above integral, we find:

$$\frac{\boldsymbol{M}_B^*}{D^*} = \left[\int_0^{L^*} x^* \left(\left. p^* \right|_{z^* = -h^*} \right) dx^* - x_0^* f_3^* \right] \boldsymbol{e_2} , \tag{A.11}$$

where $\boldsymbol{e_2}$ is the unit vector in the y-direction. After lengthy computations dropping the higher-order terms, we obtain:

$$\frac{\boldsymbol{M}_B^*}{D^*} = \rho^* \left[g^* h^* L^* \left(\frac{L^*}{2} - x_0^* \right) - g^* \sum_{n=1}^{+\infty} \frac{[1 - (-1)^n]}{(n k^*)^2} H_n^* + \frac{h^{*2}}{2} \sum_{n=1}^{+\infty} \frac{[1 - (-1)^n]}{n k^*} \dot{U}_n^* \right.$$

$$\left. + \sum_{n=1}^{+\infty} \frac{[1 - (-1)^n]}{n k^*} \sum_{m=1}^{+\infty} (m \chi^*)^{-3} [1 - (-1)^m] \, \dot{\phi}_{n,m}^* \right] \boldsymbol{e_2} .$$

The moments on the left and right walls (per unit of breadth) with respect to $\boldsymbol{r_0}$ are:

$$\frac{\boldsymbol{M}_L^*}{D^*} = - \int_{-h^*}^{\eta_L^*} \left[(\boldsymbol{r}^* - \boldsymbol{r}_0^*) \times \boldsymbol{e_1} \right] \left. p^* \right|_{x^* = 0} dz^* ,$$

$$\frac{\boldsymbol{M}_R^*}{D^*} = \int_{-h^*}^{\eta_R^*} \left[(\boldsymbol{r}^* - \boldsymbol{r}_0^*) \times \boldsymbol{e_1} \right] \left. p^* \right|_{x^* = L^*} dz^* ,$$

where $\boldsymbol{r}^* = (0, y_0^*, z^*)$ in the first integral and $\boldsymbol{r}^* = (L^*, y_0^*, z^*)$ in the latter one. Expanding the computations and collecting together all the terms at the leading order, we obtain the overall contribution along the side walls:

$$M_W^* = -\rho^* D^* \left[\frac{z_0^* F_1^*}{\rho^* D^*} - g^* \frac{h^{*2}}{2} \sum_{n=1}^{+\infty} [1 - (-1)^n] H_n^* + \frac{5}{24} h^{*4} \sum_{n=1}^{+\infty} n k^* [1 - (-1)^n] \dot{U}_n^* \right.$$

$$+ \frac{h^{*2}}{2} \sum_{n=1}^{+\infty} n k^* [1 - (-1)^n] \sum_{m=1}^{+\infty} (m\chi^*)^{-3} [1 - (-1)^m] \dot{\phi}_{n,m}^*$$

$$\left. + \sum_{n=1}^{+\infty} n k^* [1 - (-1)^n] \sum_{m=1}^{+\infty} (m\chi^*)^{-5} [1 - (-1)^m] \dot{\phi}_{n,m}^* \right] e_2 .$$

B The nonlinear term in the Kinetic Energy equation

Let us consider the nonlinear term in the kinetic energy equation (25). Then, applying the summation over all the modes, we obtain:

$$\sum_{n\in\mathbb{Z}} n U_n \sum_{p\in\mathbb{Z}} U_p U_{n-p} = \sum_{n,p\in\mathbb{Z}} n U_n U_p U_{n-p} = \sum_{n,p\in\mathbb{Z}} [(n-p) + p] U_n U_p U_{n-p} =$$

$$\sum_{n,p\in\mathbb{Z}} (n-p) U_n U_p U_{n-p} + \sum_{n,p\in\mathbb{Z}} p U_n U_p U_{n-p} = \sum_{n,s\in\mathbb{Z}} s U_n U_{n-s} U_s - \sum_{n,p\in\mathbb{Z}} p U_n U_p U_{p-n} =$$

$$- \sum_{n,s\in\mathbb{Z}} s U_n U_{s-n} U_s - \sum_{n,p\in\mathbb{Z}} p U_n U_p U_{p-n} = -2 \sum_{n,p\in\mathbb{Z}} n U_n U_p U_{n-p} ,$$

where the anti-symmetric property of U_n has been used. Comparing the last term with the second double summation, we find:

$$\sum_{n\in\mathbb{Z}} n U_n \sum_{p\in\mathbb{Z}} U_p U_{n-p} = \sum_{n,p\in\mathbb{Z}} n U_n U_p U_{n-p} = 0 .$$

References

B. C. Abrahamsen and O. M. Faltinsen. The effect of air leakage and heat exchange on the decay of entrapped air pocket slamming oscillations. *Physics of Fluids*, 23:1–17, 2011.

M. Antuono and M. Brocchini. Beyond Boussinesq-type equations: Semi-integrated models for coastal dynamics. *Phys. Fluids*, 25(016603), 2013.

M. Antuono and A. Colagrossi. The damping of viscous gravity waves. *Wave Motion*, 50:197–209, 2013.

M. Antuono, A. Colagrossi, S. Marrone, and D. Molteni. Free-surface flows solved by means of SPH schemes with numerical diffusive terms. *Comp. Phys. Comm.*, 181(3):532–549, 2010.

M. Antuono, B. Bouscasse, A. Colagrossi, and C. Lugni. Two-dimensional modal method for shallow-water sloshing in rectangular basins. *J. Fluid Mech.*, 700: 419–440, 2012a.

M. Antuono, A. Colagrossi, and S. Marrone. Numerical diffusive terms in weakly-compressible SPH schemes. *Computer Physics Communications*, 183(12):2570–2580, 2012b.

M. Antuono, A. Bardazzi, C. Lugni, and M. Brocchini. A shallow-water sloshing model for wave breaking in rectangular tanks. *Journal of Fluid Mechanics*, 746: 437–465, 2014.

B. Bouscasse, M. Antuono, A. Colagrossi, and C. Lugni. Numerical and Experimental Investigation of Nonlinear Shallow Water Sloshing. *Int. J. Nonlinear Sci. Numer. Simul.*, 14(2):123–138, 2013.

A Colagrossi, C Lugni, M Greco, and OM Faltinsen. Experimental and numerical investigation of 2D sloshing with slamming. In *19th International Workshop on Water Waves and Floating Bodies, Cartona, Italy, Mar*, pages 28–31, 2004.

A. Di Mascio, M. Antuono, A. Colagrossi, and S. Marrone. Smoothed particle hydrodynamics method from a large eddy simulation perspective. *Physics of Fluids*, 29(3):035102, 2017. doi: 10.1063/1.4978274. URL http://dx.doi.org/10.1063/1.4978274.

O. M. Faltinsen and A. N. Timokha. Asymptotic modal approximation of nonlinear resonant sloshing in a rectangular tank with small fluid depth. *J. Fluid Mech.*, 470:319–357, 2002.

O. M. Faltinsen and A. N. Timokha. *Sloshing*. Cambridge University Press, 2009.

J.M. Fonfach, T. Manderbacka, and M.A.S. Neves. Numerical sloshing simulations: Comparison between lagrangian and lumped mass models applied to two compartments with mass transfer. *Ocean Engineering*, 114:168–184, 2016. ISSN 0029-8018. doi: 10.1016/j.oceaneng.2016.01.023. URL http://www.sciencedirect.com/science/article/pii/S0029801816000342.

I. Ghamari, M. Greco, O. M. Faltinsen, and C. Lugni. Parametric Resonance of a fishing vessel with and without anti-roll tank: an experimental and numerical study. *Proceedings of the ASME 2017 Int. Conf. on Ocean, Offsh. and Arctic Engn, OMAE 2017, Norway*, 2017.

M. Greco and C. Lugni. 3-D seakeeping analysis with water on deck and slamming. Part 1: Numerical solver. *JOURNAL OF FLUIDS AND STRUCTURES*, 33:127–147, AUG 2012. ISSN 0889-9746. doi: 10.1016/j.jfluidstructs.2012.04.005.

D. F. Hill. Transient and steady-state amplitudes of forced waves in rectangular basins. *Phys. Fluids*, 39(6):1576–1587, 2003.

Y. Kim, B.W. Nam, D.W. Kim, and Y.S. Kim. Study on coupling effects of ship motion and sloshing. *Ocean Engineering*, 34(16):2176–2187, 2007. ISSN 0029-8018. doi: 10.1016/j.oceaneng.2007.03.008. URL http://www.sciencedirect.com/science/article/pii/S0029801807001175.

H. Lamb. *Hydrodynamics*. Cambridge University Press, 1945.

C. Lugni, M. Brocchini, and O. M. Faltinsen. Wave Impact Loads: The role of the flip-through. *Phys. of Fluids*, 18:122101:1–17, 2006. doi: 10.1063/1.2399077.

C. Lugni, M. Brocchini, and O. M. Faltinsen. Evolution of the air cavity during a

29

depressurized wave impact. II. The dynamic field. *Phys. of Fluids*, 22:056102:1–13, 2010a. doi: 10.1063/1.3409491.

C. Lugni, M. Miozzi, M. Brocchini, and O. M. Faltinsen. Evolution of the air cavity during a depressurized wave impact. I. The kinematic flow field. *Phys. of Fluids*, 22:056101:1–17, 2010b. doi: 10.1063/1.3407664.

C. Lugni, A. Bardazzi, O. M. Faltinsen, and G. Graziani. Hydroelastic slamming response in the evolution of a flip-through event in shallow-liquid sloshing. *Phys. of Fluids*, 26:032108:1–35, 2014. doi: 10.1063/1.4868878.

D. Molteni and A. Colagrossi. A simple procedure to improve the pressure evaluation in hydrodynamic context using the SPH. *Computer Physics Communications*, 180(6):861–872, 2009.

O. F. Rognebakke and O. M. Faltinsen. Coupling of sloshing and ship motions. *JOURNAL OF SHIP RESEARCH*, 47(3):208–221, SEP 2003. ISSN 0022-4502.

J. Veeramony and I.A. Svendsen. The flow in surf-zone waves. *Coast. Engng.*, 39: 93–122, 2000.